Ionics (2024) 30:971–978
https://doi.org/10.1007/s11581-023-05330-2

RESEARCH

emaZero-additional-energy-consumption fabrication of a self-supported electrode: synergistic redox-corroding and boronizing engineering for overall water splitting

Guanglun Sun[1] · Yuanzhe Wang[2] · Feng Chen[1] · Faming Gao[1,2]

Received: 13 November 2023 / Revised: 13 November 2023 / Accepted: 24 November 2023 / Published online: 7 December 2023

Abstract

The non-precious metal-based materials show excellent catalytic activity for overall water splitting. However, it is still a challenge to meet the requirements of fabricating catalysts with cost-effective, high-performance, and large-scale production. In this paper, we report an energy-efficient, low-cost, scaled-up redox-corroding, and boronizing engineering method for transforming inexpensive nickel foam into highly active, flexible, and durable self-supported electrodes for overall water splitting. This work adopts a desirable redox-corroding and one-pot $NaBH_4$ reduction reaction of nickel foam in aqueous solutions containing trivalent cations (Fe^{3+}) under ambient temperature. This process results in well-distributed amorphous iron–nickel borides and hydroxides active materials that are grown in situ on the surface of porous nickel foam. The $NiFeB_x$/NF//NiFe-OH/NF electrode pair shows low cell voltages of 1.63 V to achieve 10 mA cm^{-2} in 1 M KOH. More importantly, the $NiFeB_x$/NF//NiFe-OH/NF electrode exhibits ultrahigh catalytic activities at high current densities, outperforming the benchmark electrode pair of Pt-C/NF//RuO_2/NF. This inexpensive and simple controllable strategy provides Ni foam-substrate-derived electrodes with excellent catalytic activities and opens up new avenues for the rapid and simple fabrication of highly efficient electrodes for overall water splitting with large-scale applications.

Keywords Iron-nickel · Self-supported electrodes · Water splitting

Introduction

Hydrogen, due to its environmentally friendly and high gravimetric energy density characteristics, offers enormous potential to address increasing energy demands in the future [1–3]. Large-scale electrocatalytic water splitting technology is a key way to obtain high-purity hydrogen gas [4–6]. As an unfavorable reaction due to its thermodynamic barrier, water splitting always works at much larger overpotentials relative to the theoretical value [7]. The use of highly active catalysts can effectively reduce the energy barrier in hydrogen/oxygen evolution processes (HER/OER) and thus decrease the overpotential. It is known that noble metal-based materials (e.g., Pt-based and Ir/Ru-based) are the most active benchmark catalysts for water splitting. Unfortunately, their rarity and poor stability make their widespread application impractical [8, 9]. Accordingly, great efforts have been devoted to non-precious electrocatalysts using earth-enriched materials, such as hydroxides/layered double hydroxides [10–12], borides [13, 14], sulfides [15–17], carbides [18, 19], nitrides [20, 21], selenides [22–24], and phosphides [25–29].

Despite significant progress in the improvement of catalytic activity for HER/OER, notable challenges remained in using these promising non-precious electrocatalysts for large-scale and practical applications [30, 31]. On the one hand, most of the current powdered electrocatalysts can only be used when cast on the substrate with adhesives, which inevitably obstructs the active sites, increases the contact resistance, and hinders the translocation of the electrolyte to

✉ Yuanzhe Wang
wyz1610984408@163.com

✉ Faming Gao
fmgao@ysu.edu.cn

[1] Key Laboratory of Applied Chemistry, College of Environmental and Chemical Engineering, Yanshan University, Qinhuangdao 066004, People's Republic of China

[2] Tianjin Key Laboratory of Brine Chemical Engineering and Resource Ecological Utilization, Tianjin University of Science & Technology, Tianjin 300222, People's Republic of China

the active sites [32]. On the other hand, the material easily peels away from the current collector during large-current or long-term electrocatalysis for coated active materials, owing to the poor adhesive force between the active material and the current collector [33]. Thus, these electrocatalyst powders can only work at low current densities and cannot be adapted to industrial production in high current density states. As a result, to obtain more practical and highly efficient electrodes for large-scale applications, electrodes should be prepared using common materials and the strategy should be as simple as possible [34].

Currently, self-supported electrodes with active material directly growing on conductive substrates are more desirable because they offer many intrinsic properties compared with conventional powdery electrocatalysts [35, 36]. First, the direct growth of electroactive species on substrates avoids the post-coating procedure with an assistance binder and extra conductive agent, which improves the efficiency of the electrode preparation procedure and reduces the cost. Second, the binding of electroactive species and their underlying substrates offers thorough contact without an extra binder. Direct contact assures rapid electron transfer and prevents the catalyst from shedding over long-term usage. Typical synthetic strategies for self-supported electrodes include hydro/solvothermal, electrodeposition, and vapor deposition, which require additional energy inputs (heat or electricity) [37]. Therefore, the challenge of minimizing energy consumption during the preparation process, simplifying technological conditions, and fabricating highly active self-supported electrodes, particularly at large catalytic current densities, persists in large-scale applications.

In this work, we present amorphous iron-nickel borides and iron–nickel hydroxide nanostructures grown in situ on surface-redox-corroding Ni foam. The self-supported electrocatalyst has shown great superiority in terms of cost control, manufacturing strategy, energy consumption, catalytic activity, etc. Firstly, the NiFe-OH/NF self-supported electrode is grown on the low-cost commercial Ni foam via a redox-corroding aqueous solution of Fe^{3+}. Following this, the $NiFeB_x$/NF electrode could be well-obtained via a one-pot $NaBH_4$ reduction reaction. It is evident that this synthesis requires only a slice of Ni foam, a certain volume of Fe^{3+} solution, and $NaBH_4$, which is inexpensive to produce. Secondly, in the redox-corroding process, the inexpensive Ni foam not only serves as a 3D conductive current collector but also acts as a slow-releasing Ni source, which is induced by redox-corroding of Fe^{3+} in solution [38]. Therefore, it can be accomplished at room temperature without extra external environment applied, such as high temperatures, high pressures, electric fields, etc. At the same time, since the reduction reaction of $NaBH_4$ is exothermic, the subsequent boronization process can also be successfully completed at room temperature without additional heat input. More importantly, the $NiFeB_x$/NF//NiFe-OH/NF as an asymmetric electrode couple showed small cell voltages of 1.63 V to achieve 10 mA cm^{-2} in 1 M KOH, and the $NiFeB_x$/NF//NiFe-OH/NF electrode exhibited ultrahigh catalytic activities at high current densities, outperforming the benchmark electrode pair of Pt-C/NF//RuO_2/NF. The superb HER/OER activity would be attributed to the enhanced catalytic performance and electroconductivity enabled by the synergistic interaction of Ni and Fe elements in $NiFeB_x$ and NiFe-OH nanostructures [39], the full utilization of catalytically active materials, the accelerated electrolyte infiltration and generated H_2/O_2 diffusion empowered by the high porosity within the surface-redox-corroding Ni foam support, and the prominent inherent activity empowered by the amorphous native of $NiFeB_x$/NiFe-OH nanostructures. In conclusion, the self-supported electrocatalyst shows several characteristics of excellent commercial electrocatalysts: low cost, ease of fabrication, zero energy consumption, and good catalytic performance at high current densities, which is very important for large-scale practical applications.

Results and discussion

The 3D NiFe-OH/NF and $NiFeB_x$/NF self-supported electrodes were fabricated by a controllable redox-corroding and boronizing engineering strategy as well as in situ growth mode. Low-cost Ni foam not only served as a conductive current collector but also acted as a slow-releasing Ni source. Figure S1 displayed the evolution of self-supported electrode colors after room-temperature redox-corroding and boronizing engineering strategy. The significant change in colors, from initial bright silvery grey to yellow and then to silvery grey, demonstrated that the NiFe-based materials were directly grown on the surface of the Ni foam.

Scanning electron microscopy (SEM) and transmission electron microscopy (TEM) showed more detailed structural and micromorphological characteristics of the as-synthesized NiFe-OH and NiFeBx on Ni foam. Loose porous sponge-like $NiFeB_x$ were homogeneously deposited on Ni foam through the redox-corroding and boronizing engineering routes (Fig. 1a). TEM image clearly represented that the as-obtained $NiFeB_x$ samples were a sphere-like aggregated morphology enwrapped with irregularly shaped nanosheets (Fig. 1b). Furthermore, the selected area electron diffraction (SAED) pattern of $NiFeB_x$ samples (inset of Fig. 1b) was not distinct rings or dots, exhibiting an amorphous structure [40]. This is in accordance with the XRD results (Fig. 2a). The energy dispersive X-ray spectrum (EDS) elemental distributions (Fig. 1c, d, e, and f) revealed the even distribution of Ni, Fe, and B species over the surface of $NiFeB_x$/NF, indicating the uniform growth of $NiFeB_x$. In addition, amorphous NiFe-OH nanostructures were grown vertically

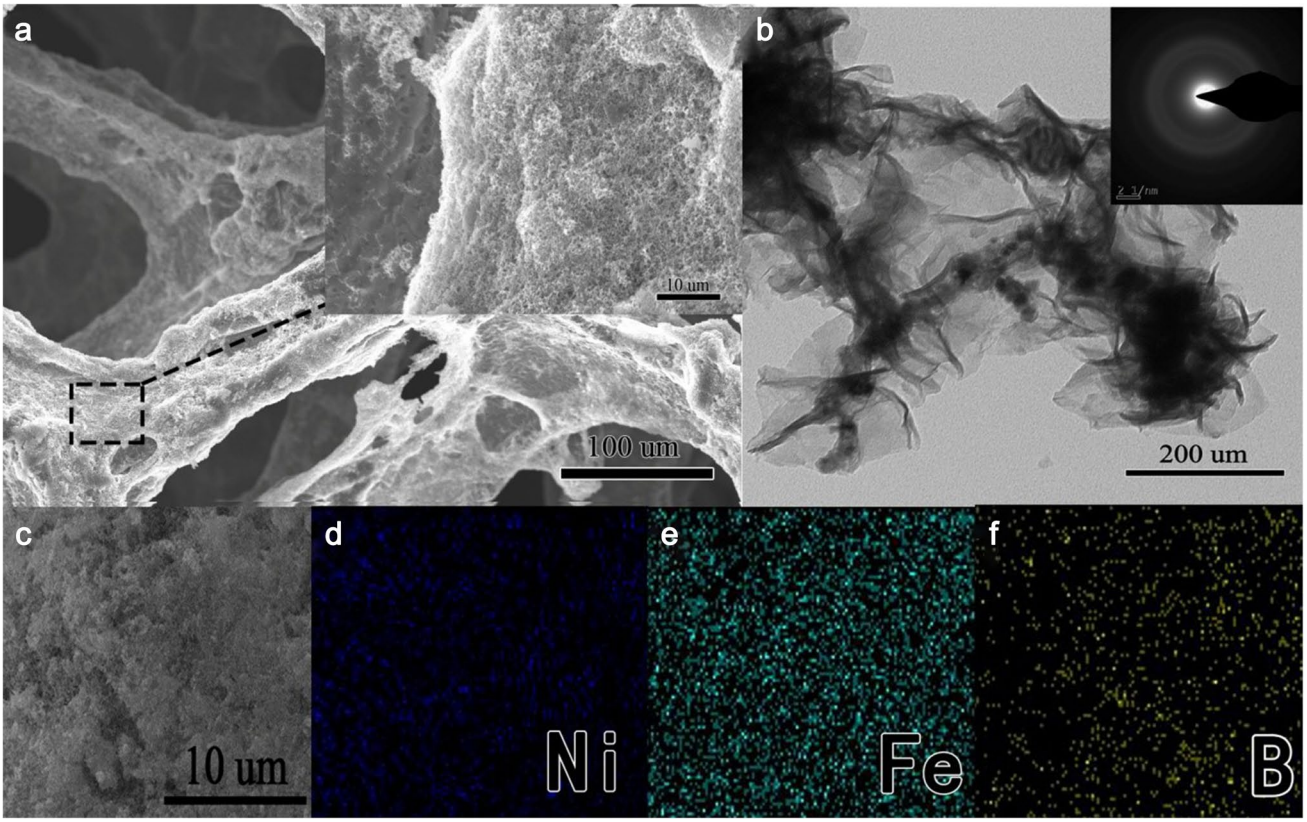

Fig. 1 **a** SEM image (inset, magnified image) of NiFeBx/NF, **b** TEM image (inset, the SAED pattern of NiFeBx) of NiFeBx, and **c** TEM images of NiFeBx/NF and the corresponding elemental mapping images of Ni (**d**), Fe (**e**), and B (**f**)

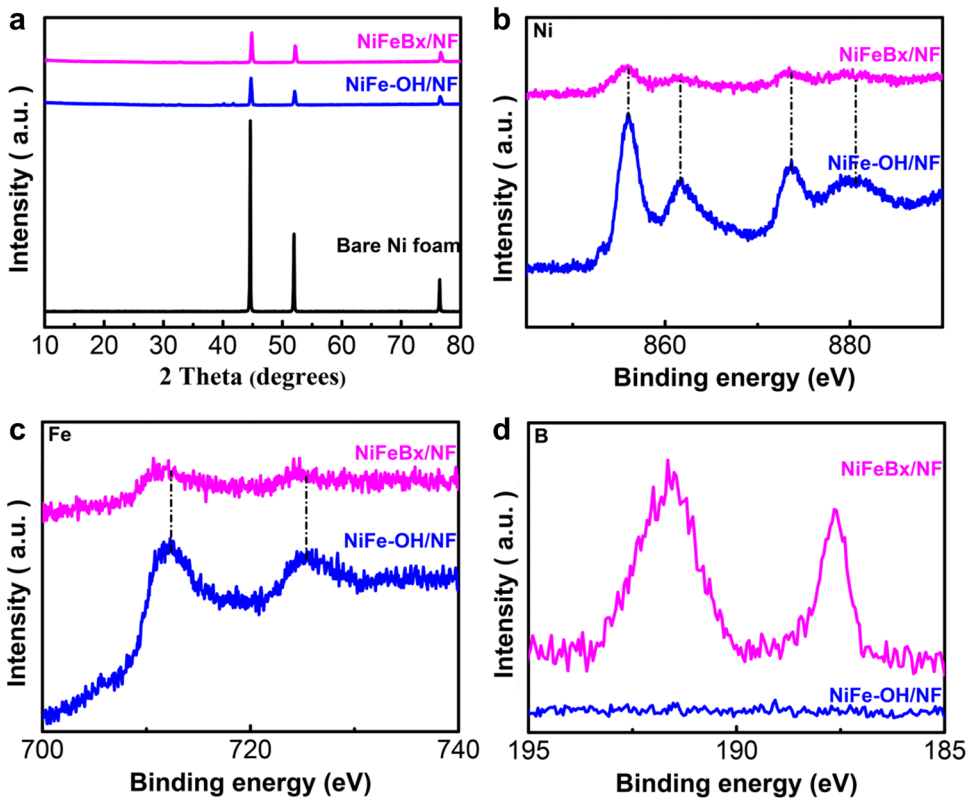

Fig. 2 **a** XRD patterns of as-prepared electrodes. XPS spectra of **b** Ni 2p, **c** Fe 2p, and **d** B 1 s peaks of NiFe-OH/NF and NiFeBx/NF

upon Ni foam with a smooth surface after redox-corroding and hydrolysis co-precipitation as shown in Figure S3. Meanwhile, deep etch marks of microcracks or holes were distinctly seen in the exposed areas of the Ni foam, while barely observed in the original area (Figure S2). They were derived from redox corroding of the added iron precursor on a Ni foam substrate. The unique architecture of $NiFeB_x$/NF and NiFe-OH/NF electrodes is expected to add contact area with the electrolyte and specific surface area, which contributes to improving catalytic activity. To investigate the structure of the as-synthesized self-supported electrode, XRD was further researched.

X-ray photoelectron spectroscopy (XPS) was utilized to deep analyze the surface chemistry of the samples [41]. The XPS spectrums of the as-obtained $NiFeB_x$/NF and NiFe-OH/NF were compared in detail (Fig. 2b, c, and d). For NiFe-OH/NF, two main peaks of Ni located at 855.8 and 874.1 eV are assigned to Ni $2p_{3/2}$ and Ni $2p_{1/2}$, respectively. In addition, the binding energy of Ni centered at 861.8 and 879.8 eV, corresponding to two satellite peaks (Fig. 2b). In the Fe 2p spectrum of NiFe-OH (Fig. 2c), the Fe $2p_{3/2}$ and Fe $2p_{1/2}$ peaks were located at binding energies of 711.8 and 724.8 eV, respectively, indicating the presence of Fe^{3+} [42]. After one-pot $NaBH_4$ reduction, boron not only formed the amorphous $NiFeB_x$ but also transferred certain electrons to transition metal atoms Ni and Fe, which led to the peak of Ni and Fe shifting to lower binding energy, providing active sites of transition metal with enriched d population, leading to excellent activity of amorphous metal borides. The B 1 s spectrum of NiFeBx was deconvoluted into two main species located at 187.8 and 191.7 eV, respectively (Fig. 2d). The former peak was ascribed to the interaction of boron with metals (Ni, Fe), while the latter was due to oxidized borate species, caused by prevalence surface oxidation of metal borides in the synthesis [43].

In addition to Ni foam, several other transition metal element substrates (such as Cu foam) can also be used effectively. Accordingly, this modulation results in the formation of CuFeBx and CuFe-OH on the surface of Cu foam (Figure S4). These results demonstrate the extensibility of redox-corroding and boronizing engineering strategies. Additionally, this redox-corroding and boronizing engineering strategy is easily scaled up. A large-area electrode (20×25 cm) comprising uniform distribution active materials has been prepared (Figure S1).

The surface hydrophilicity/hydrophobicity properties of the bare Ni foam and the as-obtained NiFe-OH/NF and $NiFeB_x$/NF were also studied. As depicted in Figure S5, it can be demonstrated that the NiFe-OH/NF and $NiFeB_x$/NF electrodes show good hydrophilicity, which contributes to better contact between electrolytes and active material. The flexibility of the NiFe-OH/NF and $NiFeB_x$/NF was further investigated by undergoing deformation and then their corresponding performances were measured (Figure S6-8). No change in catalytic activity indicated that these electrode has good mechanical flexibility.

We also studied the effects of soaking time on the resulting self-supported electrodes. Raman spectra results (Figure S9) show that well-resolved peaks appeared at 455 and 557 cm^{-1}, which might be attributed to vibrations of Ni^{2+}-OH and Ni^{2+}-O bonds in $Ni^{2+}(OH)_2$ [44, 45]. The Raman peaks were also enhanced with increasing time, indicating that the metal hydroxides can generate gradually on Ni foam as the soaking time increases [46]. However, with the instillation of $NaBH_4$, the Raman peaks weakened with increasing time (Figure S10). This indicated that under the reduction of $NaBH_4$, the hydroxide of Ni and Fe were substantially changed to amorphous $NiFeB_x$.

Combined with the above characterization consequence, it would successfully infer a rational growth mechanism of $NiFeB_x$ and NiFe-OH on Ni foam. A redox reaction between Ni foam and Fe^{3+} reacts and a large amount of Fe^{2+} and Ni^{2+} are synchronously generated near the surface of Ni foam (Eq. 1); multi-metal $NiFeB_x$ borides are successfully fabricated via a facile one-pot $NaBH_4$ reduction method [47] (Eqs. 2 and 3); (III) NiFe-OH nanostructure growth directly on Ni foam can be finally realized by the coprecipitation of Ni^{2+}, Fe^{2+}, and Fe^{3+} (Eq. 4).

$$Fe^{3+}(aq) + Ni(s) \rightarrow Fe^{2+}(aq) + Ni^{2+}(aq) \quad (1)$$

$$2Ni^{2+}(aq) + 4BH^{4-}(aq) + 9H_2O(l) \rightarrow Ni_2B(s) + 12.5H_2\,(g) + 3\,B(OH)_3 \quad (2)$$

$$2Fe^{2+}(aq) + 4BH^{4-}(aq) + 9H_2O(l) \rightarrow Fe_2B(s) + 12.5H_2\,(g) + 3\,B(OH)_3 \quad (3)$$

$$Fe^{2+}(aq) + Ni^{2+}(aq) + Fe^{3+}(aq) + OH^- \rightarrow NiFe - OH(s) \quad (4)$$

The advantages of Ni–Fe-based self-supported electrodes (well conductivity, 3D porous structure, presence of large exposed active sites, etc.) make them promising robust electrocatalysts. A typical three-electrode apparatus was used to evaluate and compare the HER performance of the Ni–Fe-based self-supported electrode in a 1 M KOH solution [48]. Figure 3a shows the linear sweep voltammetry (LSV) curves of all as-prepared electrodes. Figure s11 shows the LSV curves of the samples with different redox-corroding times in the $FeCl_3$ solution. Among the soaking durations, 1, 3, 5, and 7 h, 7 h was found to impart better activity. Notably, bare Ni foam exhibited poor HER activity, while the HER performance of the as-obtained series of $NiFeB_x$/NF and NiFe-OH/NF acquire much smaller overpotentials and larger current densities. Conversely, bare Ni foam exhibited poor HER activity. These results demonstrated that the coupling of Ni and Fe could observably improve the electrocatalytic HER performance. Among these catalysts, the $NiFeB_x$/NF

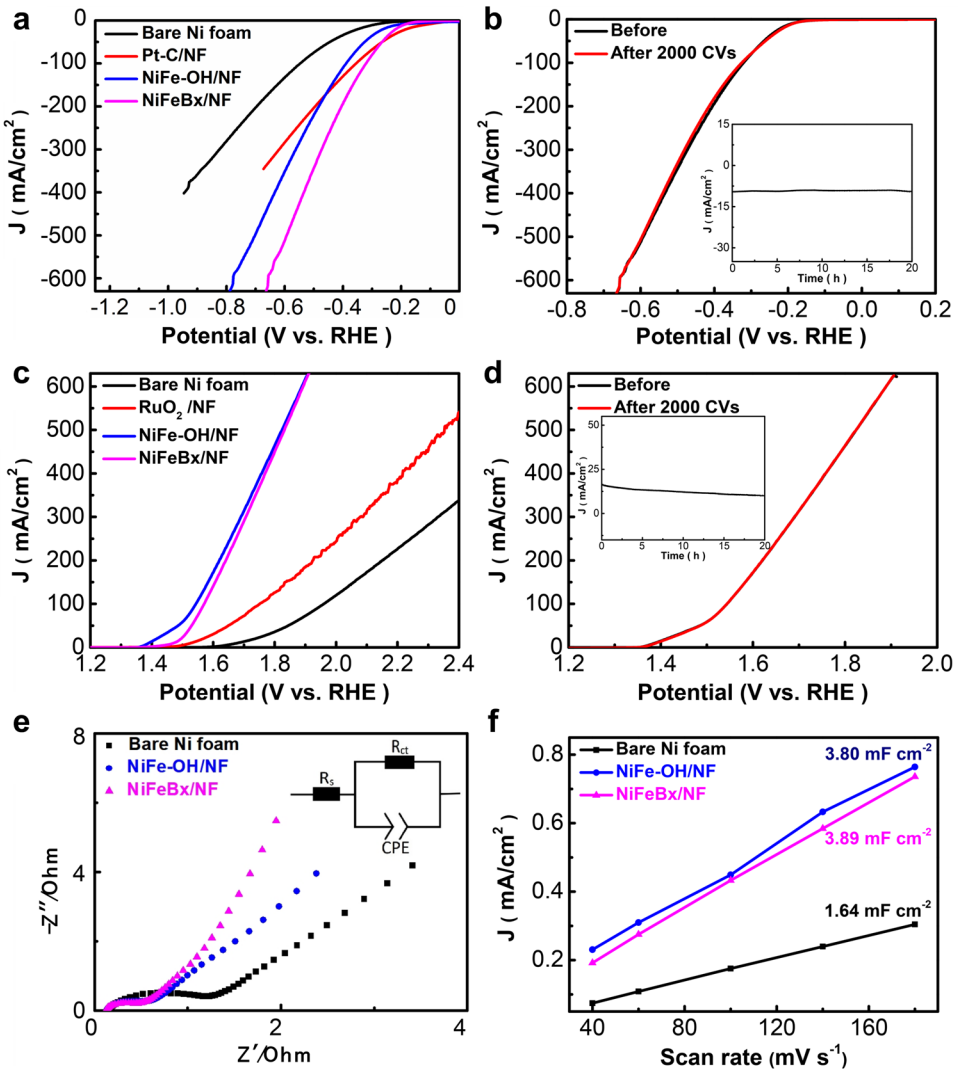

Fig. 3 **a** Polarization curves of NF, NiFe-OH/NF, NiFeBx/NF, and 20% Pt-C/NF in 1 M KOH for the HER. **b** Polarization curves for NiFeBx/NF before and after 2000 cycles. Inset, I–t curve for NiFeBx/NF under static overpotential for 20 h. **c** Polarization curves of NF, NiFe-OH/NF, NiFeBx/NF, and RuO_2/NF in 1 M KOH for the OER. **d** Polarization curves for NiFe-OH/NF before and after 2000 cycles. Inset, I–t curve for NiFe-OH/NF under static overpotential for 20 h. **e** Electrochemical impedance spectroscopy (EIS) spectra of as-prepared eletrodes. **f** Plots showing the extraction of the C_{dl}

self-supported electrode showed the highest catalytic activity. The overpotential of the $NiFeB_x$/NF self-supported electrode was 191 mV to render a current density of 10 mA cm^{-2} for HER, which was obviously lower than that of the NiFe-OH/NF (220 mV) and pure Ni foam (296 mV). This result confirmed that the incorporation of the B component could significantly increase the catalytic HER reactivity of NiFe-based materials. Furthermore, the corresponding Tafel slopes of the $NiFeB_x$/NF are also smaller than those of the NiFe–OH/NF electrode and bare Ni foam, demonstrating a more rapid reaction kinetics of the $NiFeB_x$/NF (Figure S13). In addition, a small Tafel slope is preferred for large-scale applications, and a significant increase in HER rate will be obtained as the overpotential increases [49]. The electrochemical stability of the $NiFeB_x$/NF electrode was measured by continuous cyclic voltammetry (CV) scanning of 2000 cycles (Fig. 3b). The decay of the polarization curve after 2000 cycles is negligible, thus demonstrating the excellent durability of the $NiFeB_x$/NF electrode. The durability is further verified with a long-term current-dependent time relation test. The current density of the $NiFeB_x$/NF electrode remained unchanged over a 20-h test, confirming its excellent stability.

In regard to OER, catalytic activities of the $NiFeB_x$/NF, NiFe-OH/NF, bare Ni foam, and RuO_2/NF are also assessed in the identical electrolyte to HER. Figure 3c and Figure S12 show the linear sweep voltammetry (LSV) curves of all as-prepared electrodes and the samples with different redox-corroding times in the $FeCl_3$ solution, respectively. In contrast to HER, the NiFe-OH/NF electrode possesses the optimal OER performance, with an overpotential of 160 mV to achieve a current density of 10 mA cm^{-2}, significantly lower than bare Ni foam (450 mV), $NiFeB_x$/NF (242 mV), and RuO_2/NF (298 mV). The corresponding Tafel plots in Figure S14 show that the NiFe-OH/NF catalyst owned the lowest Tafel value, further indicating its remarkable OER performance. Furthermore, both the current-dependent time relation and LSV curves after 2000 cycles showed no obvious decay (Fig. 3d), indicating the

excellent long-term OER durability of the NiFe-OH/NF electrode.

To better elucidate the origins of improved activity for $NiFeB_x$/NF and NiFe-OH/NF, electrochemical impedance spectroscopy (EIS) was performed to evaluate the electron transport ability [50]. The EIS spectra (Fig. 3e) reveal the reduced Rct values of the $NiFeB_x$/NF and NiFe-OH/NF electrodes compared to Ni foam. This trend expresses that Fe incorporation can also efficiently reduce the impedance during the charge transfer, causing a faster charge transfer rate of the $NiFeB_x$/NF and NiFe-OH/NF in the strong alkaline solution. The electrochemical active surface area (ECSA) was also calculated to measure the active area of the catalyst [51], for instance, the electrochemical double-layer capacitance (C_{dl}). The value of the $NiFeB_x$/NF (3.89 mF cm^{-2}) is similar to the NiFe-OH/NF catalyst (3.80 mF cm^{-2}), yet much higher than the bare Ni foam (1.64 mF cm^{-2}) electrode (Fig. 3f). The large ECSA of $NiFeB_x$/NF and NiFe-OH/NF can be derived from the active site NiFe-based nanostructure uniformly decorated on the surface of Ni foam and the increased number of active sites by Fe incorporation. These properties further explain the prominent electrocatalytic performance of $NiFeB_x$/NF and NiFe-OH/NF.

Encouraged by the excellent activity of both HER and OER, the overall alkaline water-splitting electrolyzer was fabricated using NiFe-OH /NF and $NiFeB_x$/NF as the anode and cathode electrode, respectively ($NiFeB_x$/NF (−)||NiFe-OH/NF (+)). A current density of 10 mA cm^{-2} can be achieved at a small cell voltage of 1.63 V (Fig. 4a), which is similar to that of $NiFeB_x$/NF||$NiFeB_x$/NF (1.628 V) and superior to those for NiFe-OH /NF||NiFe-OH/NF (1.728 V) and NF||NF (1.838 V) (Figure S15). Long-term current-dependent time relation tests for NiFeBx/NF||NiFe-OH/NF achieved a constant 20 mA cm^{-2} in 1.0 M KOH, demonstrating that this electrode couple could well maintain full water splitting over 25 h (Fig. 4b). Furthermore, during the overall alkaline water splitting process, when the current density reaches 200 mA cm^{-2}, it can be clearly seen (Fig. 4a) that the $NiFeB_x$/NF//NiFe-OH/NF electrodes are able to achieve higher current densities than the Pt-C/NF//RuO_2/NF electrodes at the same voltage. And most commercial overall water-splitting processes are accomplished under high current density conditions. This indicates that the $NiFeB_x$/NF//NiFe-OH/NF electrode is able to exhibit higher catalytic activity than the commercial electrocatalysts at high current densities, which provides the potential for its practical application.

The morphological and structural stability after electrochemical durability tests of the $NiFeB_x$/NF and NiFe-OH/NF electrodes were further explored. Figure S16 shows the largely unchanged XRD pattern of the $NiFeB_x$/NF and NiFe-OH/NF electrode before and after electrochemical durability tests, indicating the stable amorphous structures of $NiFeB_x$ and NiFe-OH. Furthermore, it is worth noting that the morphology of $NiFeB_x$/NF and NiFe-OH/NF nanostructures are well-preserved with negligible changes (Figures S17 and S18). The excellent morphology durability is attributed to the support of Ni foam with a 3D porous structure, restraining the shedding of active material and accelerating ion transport during HER/OER processes. These results suggest that the $NiFeB_x$/NF and NiFe-OH/NF electrodes have excellent stability during the HER/OER process. The mechanical flexibility of the NiFe-OH/NF and $NiFeB_x$/NF was further investigated by undergoing deformation and then their corresponding performances were measured (Figure S6-8). No change in catalytic activity indicated that this electrode has good mechanical flexibility.

To better understand the mutual effect between nickel and iron in $NiFeB_x$ for HER performance, DFT calculations were performed to focus on the changes in HER Gibbs free energy and electronic structure [52, 53]. $NiFeB_x$ is amorphous, and the amorphous structure is very complex. In order to explore the effect of iron introduction on the activity of hydrogen evolution, we took Ni_2B as a model in this experiment.

Firstly, the free energies of adsorbed H (ΔG_H) at the Ni site are presented in Fig. 5a. Obviously, the Gibbs free energy of all the H adsorption sites in the Ni site of Fe-doped Ni_2B is close to zero compared to the pristine Ni site.

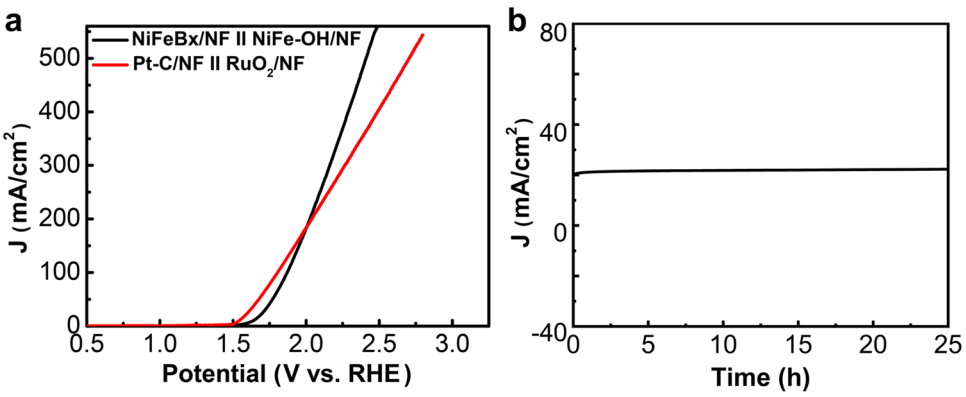

Fig. 4 **a** Polarization curves of the electrodes in 1 m KOH for overall water splitting. **b** Long-term stability test performed under static overpotential for 25 h

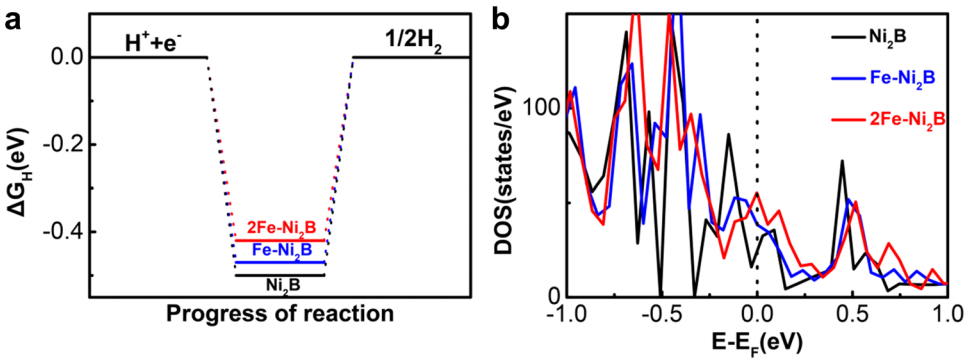

Fig. 5 **a** H* adsorption energy. and **b** density of states (DOS) of Ni_2B, Fe-Ni_2B, and 2Fe-Ni_2B systems

Furthermore, the Gibbs free energy of the H adsorption in the Ni site is closer to zero with the further introduction of iron atoms. Therefore, the presence of Fe elements promotes the activity of active sites Ni as expected.

As we know that chemical properties are intensively determined by their electronic structure, a calculation of the density of states (DOS) could provide us insight into the different HER activity [54]. As can be seen from Fig. 5b, a large number of electronic states occur near the Fermi level, suggesting that more charge carriers can be introduced by Fe atom doping compared to that of the pristine Ni_2B, thereby increasing electrical conductivity, which heavily accelerates the efficiency of $NiFeB_x$ HER catalysts. Through theoretical calculations, we found that the doping of Fe can effectively improve the activity of the catalyst, which has a certain reference value.

Conclusion

In summary, a simple room-temperature redox-corroding and boronizing engineering method was proposed for the in situ growth of $NiFeB_x$ and NiFe-OH on Ni foam ($NiFeB_x$/NF and NiFe-OH/NF). Through rational control of the preparation environment such as reaction time, it can be partially etched and converted to the Ni–Fe-based catalysts with regulated physical forms and chemical compositions at the same time. This low-cost and facile controllable strategy affords Ni foam-substrate-derived electrodes owning remarkable catalytic activities and were used as asymmetric electrodes for overall water splitting. The $NiFeB_x$/NF// NiFe-OH /NF electrode pair showed ultralow cell voltages of 1.63 V@10 mA cm^{-2} in 1 M KOH. More importantly, the $NiFeB_x$/NF//NiFe-OH/NF electrode exhibited ultrahigh catalytic activities at high current densities, outperforming the benchmark electrode pair of Pt-C/NF//RuO_2/NF. This inexpensive and simple controllable preparation strategy at room temperature provides Ni foam-substrate-derived electrodes with excellent catalytic activities and opens up new avenues for the rapid and simple synthesis of efficient electrocatalysts for overall water splitting with large-scale production.

Supplementary Information The online version contains supplementary material available at https://doi.org/10.1007/s11581-023-05330-2.

Author contributions F.G. , Y.W. and G.S. wrote the main manuscript text and F.C. prepared figures 1. All authors reviewed the manuscript.

Funding This work was supported by the Hebei Key Laboratory of Applied Chemistry after Operation Performance (grant no. 22567616H).

Data Availability Data will be made available on request.

Declarations

Competing interests The authors declare no competing interests.

References

1. Bonaccorso F, Colombo L, Yu G, Stoller M, Tozzini V, Ferrari AC, Ruoff RS, Pellegrini V (2015) Science 347:1246501
2. Shindell D, Smith CJ (2019) Nature 573:408–411
3. Dey RS, Purkait T, Kamboj N, Das M (2019) Carbonaceous Materials and Future Energy: Clean and Renewable Energy Sources, 1st edn. CRC Press. https://doi.org/10.1201/9781351120784
4. Chatenet M, Pollet BG, Dekel DR, Dionigi F, Deseure J, Millet P, Braatz RD, Bazant MZ, Eikerling M, Staffell I, Balcombe P, Shao-Horn Y, Schafer H (2022) Chem Soc Rev 51:4583–4762
5. Wang YZ, Liu SS, Hao XF, Luan SR, You HH, Zhou JS, Song DD, Wang D, Li H, Gao FM (2019) J Mater Chem A 7:10572–10580
6. Zhang A, Liang Y, Zhang H, Geng Z, Zeng J (2021) Chem Soc Rev 50:9817–9844
7. Chen S, Wang YH, Wang ZJ, Zhang K (2023) Ionics 29:9–32
8. Li C, Baek JB (2020) ACS Omega 5:31–40
9. Jiao Y, Zheng Y, Jaroniec M, Qiao SZ (2015) Chem Soc Rev 44:2060–2086
10. Liu HH, Liu SY, Cao SF, Zhang JR, Ni H, Lin XJ, Chen XD, Wei SX, Hou Q, Wang ZJ, Lu XQ (2022) ACS Sustain Chem Eng 10(21):7100–7107
11. Peng CW, Huang R, Pan GX, Liu WB, Wang L (2020) Ionics 26:301–309
12. Li XG, Liu C, Fang Z, Xu L, Lu CL, Hou WH (2022) J Mater Chem A 10:20626–20634
13. Yixin H, Zhenxiang Z, Ting L, Ping Y (2022) Int J Hydrogen Energy 47:12539–12546
14 Lewandowski M, Bartoszewicz M, Jaroszewska K, Mariadassou GD (2022) J Ind Eng Chem 116:75–98

15. Dong Y, Fang Z, Yang WY, Tang B, Liu Q, Appl ACS (2022) Mater Interfaces 14(8):10277–10287
16. Yang XN, Sui GZ, Guo DX, Chu DW, Li JL, Na SN, Yu MR, Li DQ (2023) Ionics 29:4115–4123
17. Tong Y, Chen PZ (2021) Dalton Trans 50:7776–7782
18. Wang J, Zhu R, Cheng J, Song Y, Mao M, Chen F, Cheng Y (2020) Chem Eng J 397:125481
19. Ge R, Zhao J, Huo J, Qu J, Yang J, Li Y et al (2022) Materials Today Nano 20:100248
20. Chen PZ, Feng DM, Li KX, Tong Y (2022) Dalton Trans 51:16990–16999
21. Li KX, Tong Y, Feng DM, Chen PZ (2022) J Colloid Interface Sci 622:410–418
22. Zhang L, Li Z, Lu YY, Yang S, Zhang HH, Tang JJ, Yu FL, Liu YB, Chen GJ, Zhou Y (2023) Ionics 28:1323–1335
23. Shen S, Wang Z, Lin Z, Song K, Zhang Q, Meng F, Gu L, Zhong W (2022) Adv Mater 34:2110631
24. Das M, Kumar G, Dey RS, Appl ACS (2022) Energy Mater 5:3915–3925
25. Lv XW, Xu WS, Tian WW, Wang HY, Yuan ZY (2021) Small 17:e2101856
26. Jin M, Zhang X, Shi R, Lian Q, Niu S, Peng O, Wang Q, Cheng C (2021) Appl Catal B 296:120350
27. Li KX, He JF, Guan XZ, Tong Y, Ye YT, Chen L, Chen PZ (2023) Small 19:2302130
28. Tong Y, Chen PZ (2021) Dalton Trans 50:7364–7371
29. Li KX, Tong Y, He JF, Liu XY, Chen PZ (2023) Anion-modulated CoP electrode as bifunctional electrocatalyst for anion-exchange membrane hydrazine-assisted water electrolyser. Mater Horiz 10:5277–5287. https://doi.org/10.1039/D3MH00872J
30. Xu X, Tian XM, Zhong Z, Kang LT, Yao JN (2019) J Power sources 424:42–51
31. Das M, Biswas A, Purkait T, Boruah T, Bhardwaj S, Das SK, Dey RS (2022) J Mater Chem A 10:13589–13624
32. Zhong B, Kuang P, Wang L, Yu J (2021) Appl Catal B-Environ 299:120668
33. Liu YP, Liang X, Gu L, Zhang Y, Li GD, Zou XX, Chen JS (2018) Nat Commun 9:2609
34. Pei Y, Ge YC, Chu H, Smith W, Dong P, Ajayan PM, Ye MX, Shen JF (2019) Appl Catal B Environ 244:583–593
35. Ning M, Wu L, Zhang F, Wang D, Song S, Tong T, Bao J, Chen S, Yu L, Ren ZF (2021) Mater Today Phys 19:100419
36. Das M, Kamboj N, Purkait T, Sarkar S, Dey RS (2020) J Phys Chem C 124:13525–13534
37. Sun H, Yan Z, Liu F, Xu W, Cheng F, Chen J (2020) Self-Supported Transition-Metal-Based Electrocatalysts for Hydrogen and Oxygen Evolution. Adv Mater 32:1806326. https://doi.org/10.1002/adma.201806326
38. Sun CY, Song QT, Lei JL, Li D, Li LJ, Pan FS, Appl ACS (2021) Energy Mater 4:8791–8800
39. Wang YZ, Zhou YY, Han MZ, Xi YK, You HH, Hao XF, Li ZP, Zhou JS, Song DD, Wang D, Gao FM (2019) Small 15:1805435
40. Lu X, Li YS, Tao L, Song DD, Wang YZ, Li Y, Gao FM (2019) Nanotechnology 30:055501
41. Gayathri S, Arunkumar P, Kim J, Han JH (2022) ACS Sustain Chem Eng 10(4):1689–1701
42. Liang HF, Gandi AN, Xia C, Hedhili MN, Anjum DH (2017) U Schwingenschlögl, HN Alshareef. ACS Energy Lett. 2:1035–1042
43. Li H, Wen P, Li Q, Dun C, Xing J, Lu C, Adhikari S, Jiang L, Carroll DL, Geyer SM (2017) Adv Energy Mater 7:1700513. https://doi.org/10.1002/aenm.201700513
44. Zhu KY, Zhu XF, Yang WS (2019) Angew Chem Int Ed 58:1252–1265
45. Wu YY, Li Y, Yuan MK, Hao HR, San XJ, Lv Z, Xu LL, Wei B (2022) Chem Eng J 427:131944
46. Niu SQ, Sun YC, Sun GJ, Rakov D, Li YZ, Ma Y, Chu JY, Xu P, Appl ACS (2019) Energy Mater 2:3927–3935
47 Yao R, Wu Y, Zhao Q, Li J, Liu G (2022) Int J Hydrogen Energy 47(13):8303–8313
48. Dionigi F, Zeng ZH, Sinev I, Merzdorf TS, Deshpande S, Lopez MB, Kunze S, Zegkinoglou I, Sarodnik H, Fan DX, Bergmann A, Drnec J, Araujo JF, Gliech M, Teschner D, Zhu J, Li W-X, Greeley J, Cuenya BR, Strasser P (2020) Nat Commun 11:2522
49. Yan H, Xie Y, Wu A, Cai Z, Wang L, Tian C, Zhang X, Fu H (2019) Anion-modulated HER and OER activities of 3D Ni–V-based interstitial compound heterojunctions for high-efficiency and stable overall water splitting. Adv Mater 31:1901174. https://doi.org/10.1002/adma.201901174
50. Lyu S, Guo CX, Wang JN, Li ZJ, Yang B, Lei LC, Wang LP, Xiao JP, Zhang T, Hou Y (2022) Nat Commun 13:6171
51. Huang XK, Xu XP, Li C, Wu DF, Cheng DJ, Cao DP (2019) Vertical CoP nanoarray wrapped by N, PDoped carbon for hydrogen evolution reaction in both acidic and alkaline conditions. Adv Energy Mater 9:1803970. https://doi.org/10.1002/aenm.201803970
52. Li PS, Wang MY, Duan XX, Zheng LR, Cheng XP, Zhang YF, Kuang Y, Li YP, Ma Q, Feng ZX, Liu W, Sun XM (2019) Nat Commun 10:1711
53. Yan JQ, Kong LQ, Ji YJ, White J, Li YY, Zhang J, An PF, Liu SZ, Lee ST, Ma TY (2019) Nat Commun 10:2149
54 Ouyang YX, Ling CY, Chen Q, Wang ZL, Shi L, Wang JL (2016) Chem Mater 28(12):4390–4396